CHINESE OPTICS LETTERS

Vol. 22, No. 1 | January 2024

Efficient terahertz generation from van der Waals α-In_2Se_3

Shijie Duan (段诗婕)[1,2,†], Ming Yang (杨 鸣)[1,2,†], Suyuan Zhou (周溯媛)[1,3], Longhui Zhang (张隆辉)[1,4], Jinsen Han (韩锦森)[1,2], Xu Sun (孙 旭)[1,2], Guang Wang (王 广)[1,2], Changqin Liu (刘昌勤)[1,2], Dongdong Kang (康冬冬)[1,2], Xiaowei Wang (王小伟)[1,2], Jiahao Chen (陈家浩)[1,2*], and Jiayu Dai (戴佳钰)[1,2**]

[1] Department of Physics, College of Science, National University of Defense Technology, Changsha 410073, China

[2] Hunan Key Laboratory of Extreme Matter and Applications (XMAL), Changsha 410073, China

[3] Hunan Key Laboratory for Micro-Nano Energy Materials and Devices, School of Physics and Optoelectronics, Xiangtan University, Xiangtan 411105, China

[4] Guangxi Key Laboratory of Automatic Detecting Technology and Instrument, Guilin University of Electronic Technology, Guilin 541004, China

†These authors contributed equally to this work.

*Corresponding author: chenjiahao@nudt.edu.cn

**Corresponding author: jydai@nudt.edu.cn

Received August 9, 2023 | Accepted September 6, 2023 | Posted Online January 18, 2024

Two-dimensional (2D) van der Waals materials have attracted tremendous attention due to their versatile physical properties and flexible manipulation approaches. Among the various types of van der Waals materials, α-In_2Se_3 is remarkable for its intrinsic 2D ferroelectricity and high-performance opto-electronic properties. However, the study of the α-In_2Se_3 system in terahertz (THz) radiation is scarce, although it is promising for electrically controlled THz field manipulation. We investigate the α-In_2Se_3 in different thicknesses and report that the THz generation efficiency induced by femtosecond laser pulses can be largely improved by reducing the thickness from the bulk. Furthermore, we reveal the surge current in thin film coupled with THz emission exhibits a different Auger recombination mode, which is helpful in understanding the mechanism and provides insights into the design of 2D highly efficient THz devices.

Keywords: van der Waals; terahertz; carrier dynamics.

DOI: 10.3788/COL202422.013202

1. Introduction

As graphene sparked the burst of studies in two-dimensional (2D) materials, a plethora of candidate 2D systems has been found and widely applied in opto-electronic devices. Due to the weakly bounded van der Waals (vdW) interaction between the layers, 2D materials are feasible to be exfoliated and recombined into many types of vdW heterostructures without the constraint of lattice mismatching[1]. In addition, the electronic properties can be flexibly tuned by the stacking orders[2], from intrinsic multilayer graphene[3–5] to hybrid heterostructure compositions[6], e.g., the transition metal dichalcogenides family MoS_2/WSe_2[7–9] and graphene/boron nitride (BN)[10]. Since the electronic band structure can be dramatically different at the vicinity of the surface (in contrast to the bulk state), the surface state of the vdW materials can be promising to be optimized for efficient opto-electronic devices[11–13].

Indium selenide, including InSe and In_2Se_3, is such a III–VI semiconductor that has distinguishing opto-electronic properties with a high photocurrent generation rate[14], high electron mobility[15,16], and anisotropic thermal conductivity[17–19]. A direct bandgap in the near-infrared (IR) range with a tunable bandgap close to 1.4 eV (for bulk) is found in In_2Se_3[20]. In addition, abundant phases have been identified in In_2Se_3[21–24], and in-plane (IP) and out-of-plane (OOP) ferroelectricity has been reported in α phases[25–27], while antiferroelectricity has been found in the β' phase[28]. Both α and β' phases are room temperature phases that are friendly to the manufacture of opto-electronic and memory devices.

In this work, we focus on the study of the opto-electronic properties of α-In_2Se_3 in terahertz (THz) emission and photocarrier behaviors, which is significant in improving the THz modulation efficiency by ferroelectrics. We find the intrinsic relationship between THz emission efficiency and Auger carrier dynamics in a series of different thickness samples. We propose the surface state plays a role in the surge current acceleration as well as the ultrafast Auger carrier recombination, which is enlightening in the fabrication of ferroelectric α-In_2Se_3 thin film for ideal THz performance.

© 2024 Chinese Optics Letters

2. Fabrication and Experimental Method

2.1. Sample fabrication method

The 2D layered In_2Se_3 is grown on mica substrates by the chemical vapor deposition (CVD) method using In_2Se_3 (99.99%, Alfa Aesar) powder source as the precursor and an Ar/H_2 mixture as the carrier gas. The ceramic boat, filled with the In_2Se_3 powder source, is placed in the center of a 1-inch (2.54 cm) transparent quartz tube. A freshly cleaved piece of fluorophlogopite mica is placed in the downstream about 10–15 cm away from the boat of the In_2Se_3 and serves as the substrate. The quartz tube is purged with Ar gas at a rate of 500 sccm (standard cubic centimeters per minute) for 10 min before heating, for the purpose of cleaning the gas line and removing oxygen. The temperature of the In_2Se_3 powder source is heated up to 800°C at a heating rate of 26°C/min, and then kept for 5–15 min for the growth in the atmosphere of ~3 sccm H_2 gas and ~50 sccm Ar gas. The structure and characterization details can be found in Fig. 1.

2.2. THz emission spectroscopy

THz emission spectroscopy is performed on the reflective pump-probe basis. The femtosecond amplifier pulses, characterized by a pulse width of 100 fs, a pulse energy of 4 mJ, a repetition rate of 1 kHz, and a central wavelength of 800 nm, are focused with a 45° incident angle, as indicated by Fig. 2(a). The polarization of the pulse can be continuously tuned with a half-wave plate (HWP) characterized by the angle (θ) with respect to the P polarization. The THz radiation is emitted by the free electrons excited by the pumping pulse with energy of 1.55 eV, which covers the bandgap of intrinsic α-In_2Se_3. The time-domain spectroscopy is characterized by a probe pulse assisted by the electro-optical sampling method in (110) oriented ZnTe nonlinear crystal.

2.3. Carrier reflectivity measurements

The ultrafast carrier dynamics of α-In_2Se_3 is investigated by the reflective optical pump-probe method, using a femtosecond amplifier laser system with a central wavelength of 800 nm, energy of 0.7 mJ, duration of 35 fs, and repetition rate of 10 kHz. The output pulse is split into two beams using a beam splitter. The strong pump beam is frequency doubled to 400 nm (3.10 eV) using a 200 μm β-barium borate (BBO) crystal and modulated by an optical chopper. The weak probe beam travels through a computer-controlled delay stage. As shown in Fig. 3(a), the two beams are focused and overlapped on the sample surface, and the reflected probe beam is monitored by a silicon balanced photodetector connected with a lock-in amplifier.

In this paper, we grow the sample using the CVD method by different thicknesses and prepare a bulk sample with finely polished (001) surface as a reference. We report that the THz emission pattern varies strongly with sample thickness, and the dynamics of the excited carriers indicate that the surface depletion field plays an important role in longitudinal photocurrent transfer.

3. Results and Discussion

α-In_2Se_3 exhibits a rhombohedral $R3m$ crystal structure (point group $3m$), which does not allow centrosymmetry and therefore supports the presence of spontaneous polarization from both the IP and OOP ferroelectric phase[27,29]. Figure 1(a) illustrates the 3R stacking of the α-In_2Se_3 with quintuple layers via vdW interaction. The Raman spectrum shows two characteristic broad peaks centralized at 109.1 cm^{-1} and 196.2 cm^{-1}, representing the less coherent A(LO + TO) and A(LO) phonon modes. However, the previous literature reports that β-In_2Se_3 features a 110 cm^{-1} peak for the A(LO + TO) mode[29]. Thus, we infer the multilayer nanoflakes (> 100 nm) could exhibit a mixture phase with both α and β phases. An atomic force microscopy (AFM) image in Fig. 1(c) indicates the edge thickness of the large triangular piece of α-In_2Se_3 approaches 1.28 nm and a relatively uniform surface morphology, while thicker area within the largest triangular piece grows symmetrically around the center by subtriangular stackings.

The efficiency of THz generation from wide bandgap semiconductors (> 1 eV) is normally not as high as that of narrow bandgap semiconductors (< 1 eV) due to their smaller electron mobility. However, α-In_2Se_3 exhibits a rather high electron mobility up to 2.5 $cm^2\ V^{-1}\ s^{-1}$[30,31], which could yield a large THz signal. As shown in Fig. 2(b), the dynamical range and peak field (peak–peak value) in 40 nm thin film α-In_2Se_3 are 3 times higher than that in bulk, indicating an intriguing carrier dynamics associated with surface effect. Normally, the THz emission mechanism for narrowband semiconductors is intimately connected to the nonlinear optical properties, such as optical rectification in zinc–blende type of materials[32], photo-Dember effects in doped semiconductors[33,34], photon-drag effects, and surface depletion current surge in 2D systems[35–37].

The general THz radiation mechanism induced by ultrashort pulses can be summarized by an elegant formula:

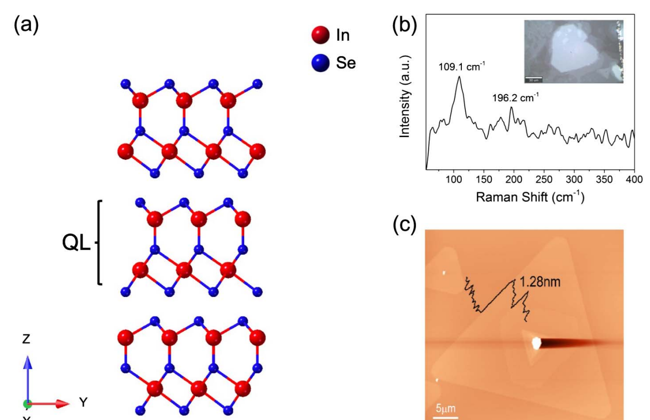

Fig. 1. Synthesis and structure characterization of α-In_2Se_3 nanoflakes. (a) Side view of the crystal structure of α-In_2Se_3 in $R3m$ space group. The quintuple layers (QLs) are stacked with weak vdW interactions. (b) Raman spectrum of α-In_2Se_3. Labeled peaks represent A(LO + TO) and A(LO) modes, respectively. (c) AFM image of the α-In_2Se_3 nanoflakes with the thickness of 1.28 nm.

$E_{\mathrm{THz}} \propto \frac{\partial^2 P}{\partial t^2} + \frac{\partial J}{\partial t}$, where P represents the nonlinear polarization that is symmetry-allowed, while J is the transient photocurrent influenced by external or internal fields. The contribution to THz radiation from the first section arises from the induced polarization associated with the crystalline symmetry, while the THz radiation from the second section can reflect the intrinsic carrier dynamics. Akin to the 2H-MoS_2 monolayer results[38], there is also a competition between optical rectification and surface current surge in α-In_2Se_3, which can be evidenced by Figs. 2(c) and 2(d), where incident polarization dependence in Fig. 2(c) exhibits twofold symmetry, and negligible azimuthal dependence in Fig. 2(d) indicates the large surge current contribution.

By a simple mathematical derivation on the nonlinear second-order susceptibility tensor for point group $3m$, which can refer to the supplementary information of a reference of MoS_2[39] that shares the same point group as α-In_2Se_3, the incident polarization dependence of the THz radiation amplitude can be simplified as

$$E_{\mathrm{THz}} \propto A \cos\theta + B \sin\theta + C \cos(2\theta) + D \sin(2\theta) + E, \tag{1}$$

where A, B, C, D, and E are coefficients associated with the nonzero components of the second-order susceptibility tensor d_{22}, d_{15}, d_{31}, and d_{33}. Likewise, the azimuthal angle dependence of the THz amplitude can be written as

$$E_{\mathrm{THz}} \propto \cos\alpha_{\mathrm{in}}(d_{22}\sin(3\phi) - 2d_{15}) + \sin\alpha_{\mathrm{in}}(d_{31} + d_{33}). \tag{2}$$

Here the optimized incident angle α_{in} is found at 45°. The measuring geometry is shown in Fig. 2(a); the incident polarization dependence is obtained by fixing the THz polarization along the x axis through a wire grid polarizer (WGP) while rotating the linear polarization angle of the incident beam through an HWP. By fitting the THz amplitude signal with Eq. (1), an explicit twofold period on the θ can well describe the optical rectification process.

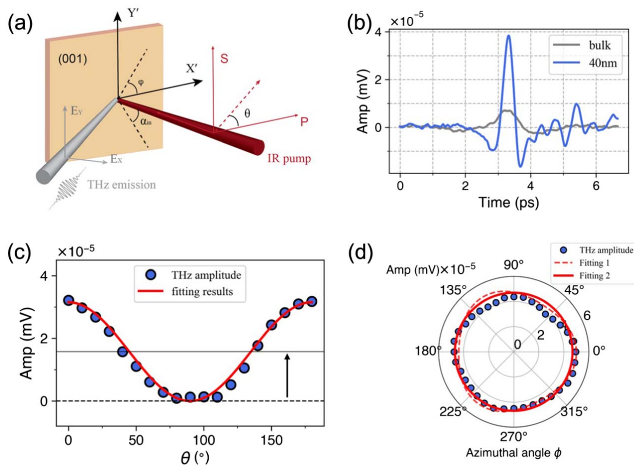

Fig. 2. THz generation from thin film and bulk α-In_2Se_3. (a) indicates the detection geometry pumped by 800 nm pulse. The incident pulse polarization angle θ and sample azimuthal angle ϕ within the *ab* plane are two degrees of freedom in studying the emitted THz properties. (b) Characterization of THz pulses from 40 nm thin film (blue) and bulk (gray) as a reference. (c) Polarization dependency of the THz pulse peak intensity and fitting by Eq. (1). (d) Azimuthal angle dependence of the THz amplitude with two types of fittings according to Eq. (2).

In addition to the optical rectification occurring in the broken surface symmetry, a large signal from the surge current cannot be ignored. The contribution of the surge current part can be explained by two possibilities: (1) the photoexcited carriers accelerated by the surface depletion field; (2) the diffusion velocity difference from electrons and holes, which is also called the photo-Dember effect. Here we tend to take the first type of photocurrent surge by surface depletion field, since the mobility of electrons and holes in the α-In_2Se_3 is comparable to MoS_2 with the same order. On the other hand, the large current shift in Fig. 2(c) from zero base line (dashed) indicated by the arrow suggests the existence of the depletion field, since the static component $E = -2\cos\alpha_{\mathrm{in}} d_{31} + \sin\alpha_{\mathrm{in}} d_{33}$ in Eq. (1) prevails at a 45° incidence. Moreover, we demonstrate two types of fitting curves to the azimuthal-dependent map according to the Eq. (2), as shown in the dashed and solid red lines. By considering the threefold component in Eq. (2) (labeled as Fitting 1), the relation of $d_{22}/(d_{31} + d_{33}) < 10$ is valid by a least-mean-square type of fitting, suggesting the static component dominates and exhibits a nearly isotropic pattern in azimuthal dependence, depicted by the solid red curve when taking d_{22} to be negligible (labeled as Fitting 2).

After examining the THz properties from the α-In_2Se_3, it is inevitable that we should investigate the photoexcited carrier dynamics, whose behavior can largely modify the THz radiation and can further assist in discriminating the different mechanisms found for bulk and thin-film states. It is significant to understand why a higher THz generation efficiency is found for films rather than bulk, which can provide guidance for THz sensor design. The carrier dynamics is depicted by the pump-probe reflectivity measurements, as shown in Fig. 3. The free carriers are generated by second harmonic generation (SHG) light in the UV region while being probed by IR. The reflectivity of the IR probe changes due to the transient generation and relaxation of the carrier density induced by photoexcitation. Figure 3(b) describes the reflectivity change from the bulk α-In_2Se_3 surface with a fine-polished (001) plane. The differences in reflectivity, represented by ΔR, increase with the pump fluence. Meanwhile, the signals after the peaks also drop more quickly at higher pumping fluence, indicating increased decaying rates. Similar features are also found in the thin-film samples of subplots Figs. 3(c)–3(e). For the smaller than 5 nm samples, as shown in subplot Fig. 3(f), the increment of the reflectivity is negligible, while a dramatic change of carrier bleaching is observed in all the pumping series.

Multiple-carrier recombination can roughly be described by different types of Auger processes, the decay time of which becomes shorter as the pump fluence increases. On the one hand, when one electron transfers the energy to another electron by recombining with a hole, it is normally called three-carrier

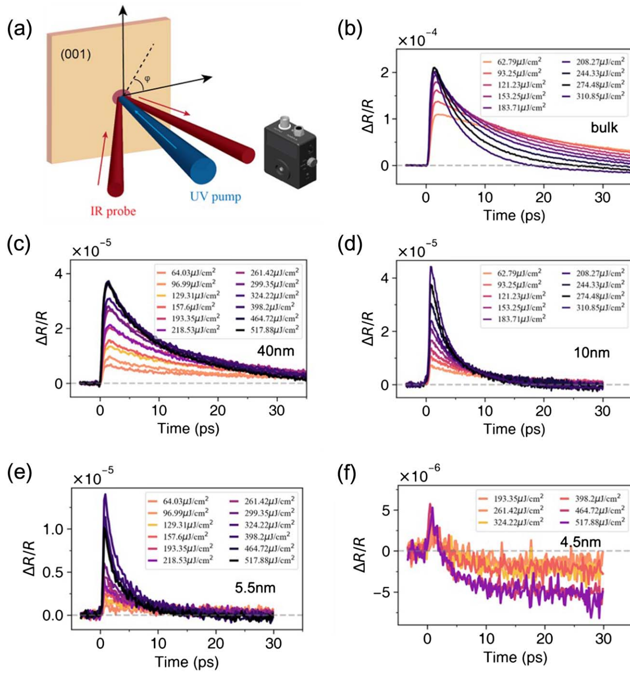

Fig. 3. Carrier dynamics investigated by reflective optical pump-probe method. (a) Schematic diagram of the measuring geometry. The UV pump beam (400 nm) and the IR probe beam (800 nm) are focused and overlapped on the sample surface with a spot size of 141 and 114 μm, respectively. The reflected signal is monitored by a silicon-balanced photodetector. (b), (c) Time-resolved reflectivity change $\Delta R/R$ of bulk and thin film α-In_2Se_3 as a function of pump-probe time delay at different pump fluence; (d)–(f) signal of reflectivity from thin films with decreased thickness of 10, 5.5, and 4.5 nm.

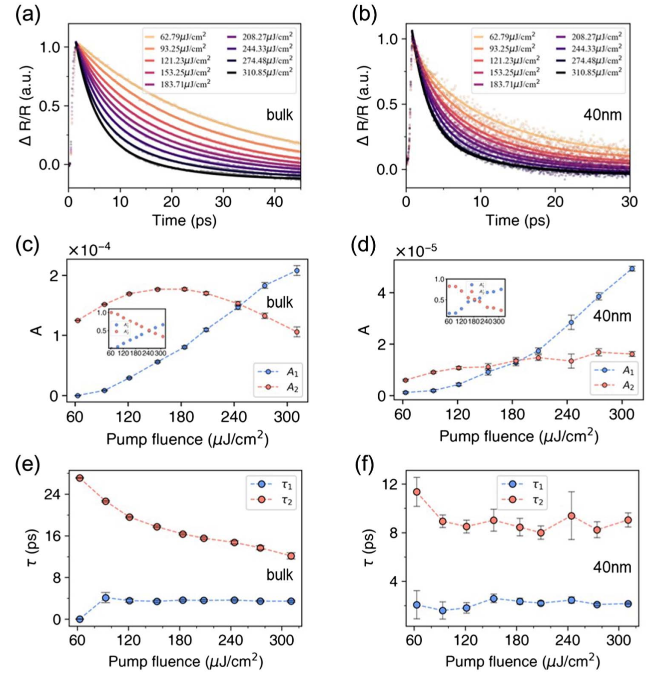

Fig. 4. Parameters of carrier dynamics retrieved from reflectivity decaying data. Left (a), (c), (e) are obtained from reference bulk sample. Right (b), (d), (f) are derived from thin-film sample. Normalized reflectivity data from (a) bulk and (b) 40 nm thin film. Dashed curves in (c) and (d) describe the amplitudes of fast (blue) and slow (red) decay varying along with pump fluence intensity. The relative amplitudes are shown in the insets. Dashed curves in (e) and (f) represent time constant change from fast (blue) and slow (red) decay at series of pump fluence.

Auger recombination. On the other hand, when an exciton is induced by photoexcitation (electron–hole pair), the energy can transform to another exciton, known as bimolecular Auger recombination. As reported in a related study by Tao *et al.*[40], the dominant recombination type can gradually switch from three-carrier to bimolecular while the sample thickness increases. However, in our analysis, we use a double-exponential fitting approach to extrapolate the recombination process, which could potentially affect the THz emission.

Figure 4 shows that the fluence-dependent decay rates from both bulk (left columns) and thin-film (right columns) states of α-In_2Se_3 are obtained by double-exponential fittings by the following equation:

$$\frac{\Delta R(t)}{R} = A_1 e^{-\frac{t}{\tau_1}} + A_2 e^{-\frac{t}{\tau_2}}, \tag{3}$$

where A_1 (A_2) and τ_1 (τ_2) represent the amplitude and time constant of the short (long) relaxation procedures. The decaying parts are normalized by the maximum of $\Delta R/R$ and are shown in Figs. 4(a) and 4(b). The relative ratios of fast (A_1') and slow (A_2') procedures are modulated by the pump fluence, as shown in the inset of Fig. 4(c) for bulk and Fig. 4(d) for thin film. The decaying procedure is dominated by long decay in the case of low pump fluence. The equilibrium pumping point of A_1' and A_2' for bulk is larger than that of the thin film, indicating a large amount of conduction-band carriers are found in bulk, as the total carrier density is induced by higher-power pumping. The fast decay time τ_1 is around 4 and 2 ps for the thin film and bulk sample, respectively. Here we infer the fast decaying part to be three-carrier Auger process, which is believed to reside around 1 to 6.5 ps[40], while the slower decaying part behaves like the bimolecular process. The decaying time constants τ from all Auger processes drop while increasing the pump fluence, as shown in Figs. 4(e) and 4(f) (the exception is the first point of τ_1 where a single exponential curve gives the best fitting). This is not surprising, since both the three-carrier and bimolecular processes comply with the relation[40] of $\tau_\beta = \frac{1}{C_\beta n(0)^{\beta-1}}$, where $\beta = 2, 3$ represents the bimolecular or three-carrier case and $n(0)$ is the transient carrier density induced by optical pumping.

When reducing the sample thickness to sub-40 nm, in contrast to the bulk case, the surface state may assist in trapping one hole and recombining it with an electron in the conduction band while transferring the energy to another free electron. This phenomenon has been reported in ZnO and CdSe nanocrystals[41,42]. The three-carrier Auger recombination has a higher probability of occurring in thinner materials, while the bimolecular case becomes more common in bulk samples when

the surface-to-volume ratio decreases. According to the measurements in Fig. 4, the faster three-carrier Auger process dominates in thin film when increasing the pumping energy, which likely accounts for the high intensity THz generation in the thin film. Another possible explanation may arise from band structure deformation while decreasing from bulk to nanoflake. Assuming that the bandgap difference is negligible under the case of strong pumping[20], the same number of free carriers moves dramatically differently in bulk and thin-film bands. For the bulk case, more free carriers move within the conduction band with slow group velocity (as indicated by the high proportion of bimolecular Auger behavior). However, the free electrons moving in discretized conduction energy levels in thin film may drop to the next energy level by the meV energy difference with a much higher group velocity, in contrast to the smoothing conduction band movement in bulk. This may explain why the current surge by a large surface depletion field is found in thin film, as indicated by the enhanced THz field emission.

4. Conclusion

We report the study of THz emission from an interesting vdW material α-In_2Se_3 and its carrier properties in thin-film and bulk states. We find the THz emission efficiency is increased by 3 times when reducing the thin-film thickness to sub-40 nm, in contrast to the bulk state. We further investigate the carrier dynamical difference between bulk and thin-film states by pump-probe reflectivity measurements and extrapolate the key decaying parameters of the free carriers induced by pumping. We argue that the three-carrier Auger process tends to dominate the electron–hole pair recombination more in thin film than in bulk, which provides a faster recombination in less than 4 ps. This phenomenon could be accompanied with a fast current surge induced by the surface depletion field in thin film, which enhances the efficiency of THz emission. Our study provides a new strategy for studying THz radiation through carrier analysis and can be exploited to investigate other vdW families.

Acknowledgements

This work was supported by the National Key R&D Program of China (No. 2017YFA0403200), the NSAF (No. U1830206), the Science and Technology Innovation Program of Hunan Province (No. 2021RC4026), and the National Natural Science Foundation of China (NSFC) (No. 62005058).

References

1. A. Castellanos-Gomez, X. Duan, Z. Fei, *et al.*, "Van der Waals heterostructures," Nat. Rev. Methods Primers **2**, 58 (2022).
2. A. K. Geim and I. V. Grigorieva, "Van der Waals heterostructures," Nature **499**, 419 (2013).
3. F. Schwierz, "Graphene transistors," Nat. Nanotechnol. **5**, 487 (2010).
4. N. O. Weiss, H. Zhou, L. Liao, *et al.*, "Graphene: an emerging electronic material," Adv. Mater. **24**, 5782 (2012).
5. H. Wu, X. Yu, M. Zhu, *et al.*, "Direct visualization and manipulation of stacking orders in few-layer graphene by dynamic atomic force microscopy," J. Phys. Chem. Lett. **12**, 7328 (2021).
6. P. Kaur, A. Boes, G. Ren, *et al.*, "Hybrid and heterogeneous photonic integration," APL Photonics **6**, 061102 (2021).
7. T. Roy, M. Tosun, X. Cao, *et al.*, "Dual-gated MoS_2/WSe_2 van der Waals tunnel diodes and transistors," ACS Nano **9**, 2071 (2015).
8. G. W. Shim, K. Yoo, S.-B. Seo, *et al.*, "Large-area single-layer $MoSe_2$ and its van der Waals heterostructures," ACS Nano **8**, 6655 (2014).
9. J. H. Yu, H. R. Lee, S. S. Hong, *et al.*, "Vertical heterostructure of two-dimensional MoS_2 and WSe_2 with vertically aligned layers," Nano Lett. **15**, 1031 (2015).
10. J. Xue, J. Sanchez-Yamagishi, D. Bulmash, *et al.*, "Scanning tunnelling microscopy and spectroscopy of ultra-flat graphene on hexagonal boron nitride," Nat. Mater. **10**, 282 (2011).
11. Y. Liu, N. O. Weiss, X. Duan, *et al.*, "Van der Waals heterostructures and devices," Nat. Rev. Mater. **1**, 16042 (2016).
12. Y. Wu, Q. Wu, F. Sun, *et al.*, "Emergence of electron coherence and two-color all-optical switching in MoS_2 based on spatial self-phase modulation," Proc. Natl. Acad. Sci. **112**, 11800 (2015).
13. L. Braun, G. Mussler, A. Hruban, *et al.*, "Ultrafast photocurrents at the surface of the three-dimensional topological insulator Bi_2Se_3," Nat. Commun. **7**, 13259 (2016).
14. J. Zhou, Q. Zeng, D. Lv, *et al.*, "Controlled synthesis of high-quality monolayered α-In2Se_3 via physical vapor deposition," Nano Lett. **15**, 6400 (2015).
15. W. Zheng, T. Xie, Y. Zhou, *et al.*, "Patterning two-dimensional chalcogenide crystals of Bi_2Se_3 and In_2Se_3 and efficient photodetectors," Nat. Commun. **6**, 6972 (2015).
16. S. Poncé, W. Li, S. Reichardt, *et al.*, "First-principles calculations of charge carrier mobility and conductivity in bulk semiconductors and two-dimensional materials," Rep. Prog. Phys. **83**, 036501 (2020).
17. C.-L. Hsin, J.-H. Huang, P. Spiewak, *et al.*, "Anisotropy of thermal conductivity in In_2Se_3 nanostructures," Appl. Surf. Sci. **494**, 867 (2019).
18. A. Rai, V. K. Sangwan, J. T. Gish, *et al.*, "Anisotropic thermal conductivity of layered indium selenide," Appl. Phys. Lett. **118**, 073101 (2021).
19. J. Han, Q. Zeng, K. Chen, *et al.*, "Lattice thermal conductivity of monolayer InSe calculated by machine learning potential," Nanomaterials **13**, 1576 (2023).
20. F. Lyu, Y. Sun, Q. Yang, *et al.*, "Thickness-dependent band gap of α-In_2Se_3: from electron energy loss spectroscopy to density functional theory calculations," Nanotechnology **31**, 315711 (2020).
21. J. van Landuyt, G. van Tendeloo, and S. Amelinckx, "Phase transitions in In_2Se_3 as studied by electron microscopy and electron diffraction," Phys. Status Solidi. A **30**, 299 (2010).
22. S. Popović, B. Čelustka, and D. Bidjin, "X-ray diffraction measurement of lattice parameters of In_2Se_3," Phys. Status Solidi A **6**, 301 (1971).
23. S. Popović, A. Tonejc, B. Gržeta-Plenković, *et al.*, "Revised and new crystal data for indium selenides," J. Appl. Crystallogr. **12**, 416 (1979).
24. K. Osamura, Y. Murakami, and Y. Tomiie, "Crystal structures of α-and β-indium selenide, In_2Se_3," J. Phys. Soc. Japan **21**, 1848 (1966).
25. W. Ding, J. Zhu, Z. Wang, *et al.*, "Prediction of intrinsic two-dimensional ferroelectrics in In_2Se_3 and other III_2–VI_3 van der Waals materials," Nat. Commun. **8**, 14956 (2017).
26. Y. Zhou, D. Wu, Y. Zhu, *et al.*, "Out-of-plane piezoelectricity and ferroelectricity in layered α-In_2Se_3 nanoflakes," Nano Lett. **17**, 5508 (2017).
27. C. Cui, W.-J. Hu, X. Yan, *et al.*, "Intercorrelated in-plane and out-of-plane ferroelectricity in ultrathin two-dimensional layered semiconductor In_2Se_3," Nano Lett. **18**, 1253 (2018).
28. C. Xu, J. Mao, X. Guo, *et al.*, "Two-dimensional ferroelasticity in van der Waals β'-In_2Se_3," Nat. Commun. **12**, 3665 (2021).
29. Y. Zhou, D. Wu, Y. Zhu, *et al.*, "Out-of-plane piezoelectricity and ferroelectricity in layered α-In_2Se_3 nanoflakes," Nano Lett. **17**, 5508 (2017).
30. J. Zhou, Q. Zeng, D. Lv, *et al.*, "Controlled synthesis of high-quality monolayered α-In_2Se_3 via physical vapor deposition," Nano Lett. **15**, 6400 (2015).
31. R. Wang, T. Wang, Y. Zhou, *et al.*, "Layer-dependent ultrafast dynamics of α-In_2Se_3 nanoflakes," 2D Mater. **6**, 35034 (2019).

32. A. Rice, Y. Jin, X. F. Ma, *et al.*, “Terahertz optical rectification from ⟨110⟩ zinc-blende crystals,” Appl. Phys. Lett. **64**, 1324 (1994).
33. V. Apostolopoulos and M. E. Barnes, “THz emitters based on the photo-Dember effect,” J. Phys. D Appl. Phys. **47**, 374002 (2014).
34. P. Gu, M. Tani, S. Kono, *et al.*, “Study of terahertz radiation from InAs and InSb,” J. Appl. Phys. **91**, 5533 (2002).
35. P. A. Obraztsov, N. Kanda, K. Konishi, *et al.*, “Photon-drag-induced terahertz emission from graphene,” Phys. Rev. B **90**, 241416 (2014).
36. L. Zhang, Y. Huang, L. Zhu, *et al.*, “Polarized THz emission from in-plane dipoles in monolayer tungsten disulfide by linear and circular optical rectification,” Adv. Opt. Mater. **7**, 1801314 (2019).
37. J. Maysonnave, S. Huppert, F. Wang, *et al.*, “Terahertz generation by dynamical photon drag effect in graphene excited by femtosecond optical pulses,” Nano Lett. **14**, 5797 (2014).
38. Y. Huang, L. Zhu, Z. Yao, *et al.*, “Terahertz surface emission from layered MoS_2 crystal: competition between surface optical rectification and surface photocurrent surge,” J. Phys. Chem. C **122**, 481 (2018).
39. Y. Huang, L. Zhu, Q. Zhao, *et al.*, “Surface optical rectification from layered MoS_2 crystal by THz time-domain surface emission spectroscopy,” ACS Appl. Mater. Interfaces **9**, 4956 (2017).
40. X. Tao, E. Mafi, and Y. Gu, “Ultrafast carrier dynamics in single-crystal In_2Se_3 thin layers,” Appl. Phys. Lett. **103**, 193115 (2013).
41. T. Okuhata, T. Katayama, and N. Tamai, “Ultrafast and hot electron transfer in CdSe QD-Au hybrid nanostructures,” J. Phys. Chem. C **124**, 1099 (2020).
42. I. Robel, B. A. Bunker, P. V. Kamat, *et al.*, “Exciton recombination dynamics in CdSe nanowires: bimolecular to three-carrier Auger kinetics,” Nano Lett. **6**, 1344 (2006).